Macromolecules

Article

Cite This: Macromolecules 2018, 51, 8729−8737

pubs.acs.org/Macromolecules

Structural Unit of Polymer Crystallization in Dilute Solution As Studied by Solid-State NMR and ^{13}C Isotope Labeling

Shijun Wang,[†] Shichen Yuan,[†] Wei Chen,[‡] Yang Zhou,[†] You-lee Hong,*[,§] and Toshikazu Miyoshi*[,†]

[†]Department of Polymer Science, The University of Akron, Akron, Ohio 44325-3909, United States

[‡]State Key Lab of Pollution Control and Resource Reuse Study, College of Environmental Science and Engineering, Tongji University, Shanghai 200092, China

[§]RIKEN CLST-JEOL Collaboration Center, RIKEN, Yokohama, Kanagawa 230-0045, Japan

Supporting Information

ABSTRACT: The nucleation and growth mechanisms of semicrystalline polymers during crystallization in dilute solutions have been debated in the past decades. Wang et al. recently reported that ^{13}C CH_3 labeled poly(L-lactic acid) (PLLA), with small weight-average molecular weight $\langle M_w \rangle$ = 46K g/mol (*s*), adopted three-dimensional nanoclusters via adjacent re-entry folding in the solution-grown crystals, and its mean size was independent of crystallization temperature (T_c) [*Macromolecules* **2017**, *50*, 6404−6414]. In this work, ^{13}C CH_3 labeled PLLA chains with middle and large $\langle M_w \rangle$ of 90K g/mol (*m*) and 326 K g/mol (*l*), respectively, were synthesized. Both $\langle M_w \rangle$ and kinetics effects on the chain-folding structures and crystal habits of the ^{13}C CH_3 labeled PLLA were systematically investigated by solid-state (ss) NMR and atomic force microscopy (AFM). *s*-, *m*-, and *l*-PLLAs commonly adopted faceted lozenge single crystals in dilute amyl acetate (AA) solution (0.05 wt %) under a very low supercooling, ΔT = 40 °C, but dendrites with multiple layers under a rapidly quenched condition, ΔT = ∼130 °C. By comparison of the experimental and simulated $^{13}C-^{13}C$ DQ buildup curves, it was indicated that (i) all *s*-, *m*-, *l*-PLLA adopted the same mean structure of the three-dimensional nanoclusters in multiple rows via adjacent re-entry structure in the lozenge shape and dendrite crystals and (ii) the mean size of the nanocluster was smaller than the nanocluster size expected from the smallest $\langle M_w \rangle$ used in this study. On the basis of the crystal habits as well as dimension and size of the nanoclusters, it was suggested that (i) the PLLA chains with different $\langle M_w \rangle$s initially adopted the same nanoclusters via folding (stage I) and (ii) the aggregation process of the nanoclusters, which was dominated by kinetics, resultantly led to the different morphological features as a function of ΔT (stage II).

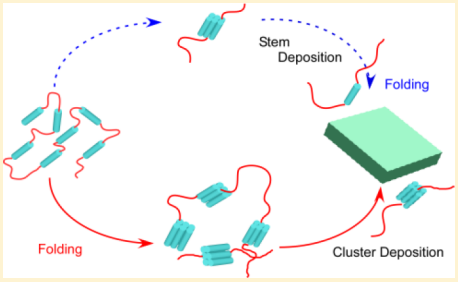

1. INTRODUCTION

Long semicrystalline polymers adopt random coils in dilute solution, and supercooling (ΔT) induces polymer crystallization generating a very thin single crystal layer.[1−4] By measuring the radius of gyration (R_g) of polymer chains in the solution state, it is recognized that long polymer chains are well folded in the single crystals.[5,6] Lauritzen and Hoffman (LH) proposed kinetically dominant "*sequence-stem deposition*" on the growth front (secondary nucleation).[7−9] It is believed that order−disorder in the chain-folding structure leads to morphological differences as a function of kinetics. On the other hand, Allegra and Meille[10,11] and Muthukumar et al.[12,13] proposed the importance of primary nucleation, where polymer chains initially form the nanoclusters via folding, so-called, bundle, followed by aggregation of the nanoclusters. To minimize surface free energy of the folded clusters, different chain-folding structures are expected in primary and secondary nucleation. Therefore, understanding the chain-level structure of semicrystalline polymers is one of the fundamental and main issues in polymer crystallization and has been studied by various techniques including neutron scattering (NS),[5,6,14−16] infrared (IR) spectroscopy,[17−19] atomic force microscopy (AFM),[20−23] and decoration methods with transmission electron microscopy (TEM).[24] Most works support adjacent re-entry rich structure in the solution-grown crystals.[5,16,20,21,24] However, the detailed chain-folding structures including folding pattern as well as successive adjacent re-entry number have been debatable matters.[5,6,14,15,17−19]

Recently, our group applied $^{13}C-^{13}C$ double quantum (DQ) NMR[25−27] to trace short-range chain trajectory of the ^{13}C selectively labeled chains via accumulating weak $^{13}C-^{13}C$ dipolar interactions.[28−37] The DQ signals allow one to determine the local folding structures including re-entrance site, a mean value of successive adjacent re-entry number, $\langle n \rangle$, and fraction, $\langle F \rangle$.[28−37] Additionally, a very tiny isotope effect of $^{13}C/^{12}C$ and smaller labeling ratio on a single site of the

Received: September 10, 2018
Revised: October 21, 2018
Published: October 26, 2018

DOI: 10.1021/acs.macromol.8b01950
Macromolecules 2018, 51, 8729−8737

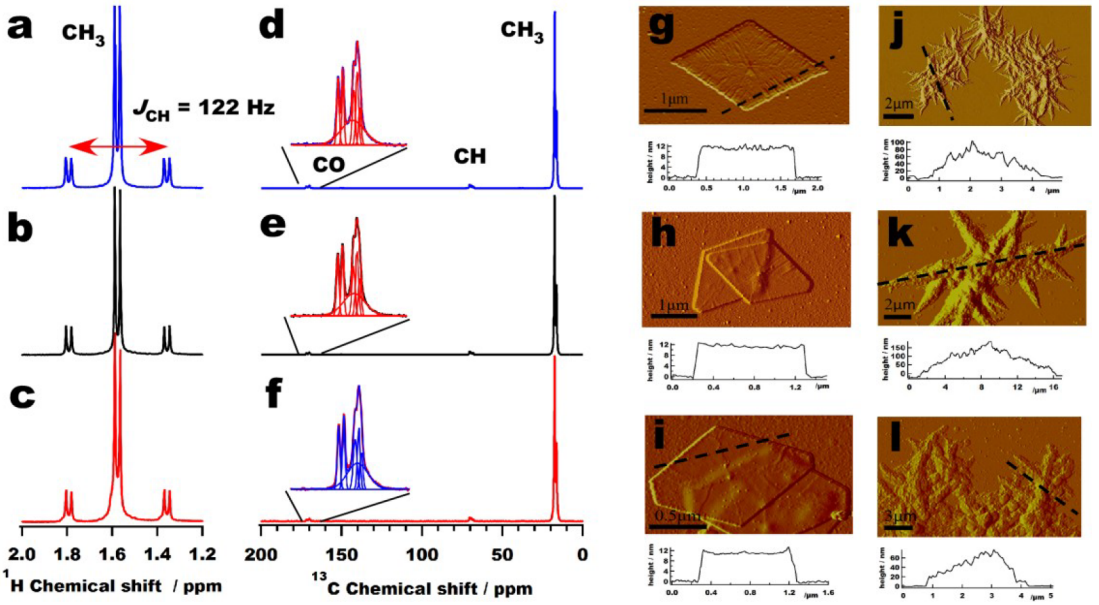

Figure 1. ^{1}H solution-state NMR spectra for the CH_3 signals of ^{13}C CH_3 labeled *s*- (a), *m*- (b), and *l*-PLLA (c) in $CDCl_3$ solution, with J_{HH} = 7 Hz and J_{CH} = 122 Hz. The ^{13}C CPMAS NMR spectra for ^{13}C 30% CH_3 labeled *s*- (d), *m*- (e), and *l*-PLLA (f) samples crystallized at 90 °C in AA solution and the corresponding CO signals with Gaussian peaks. The AFM morphological and height images for *s*- (g, j), *m*- (h, k), and *l*-PLLA (i, l) solution-grown crystals in AA solution at T_c = 90 °C (g–i) and ∼0 °C (j–l).

monomer unit naturally induces cocrystallization of ^{13}C labeled and nonlabeled polymers even under a low supercooling (ca. ΔT = 40 °C). Consequently, a wide supercooling effect on the chain-folding structure of semicrystalline polymers has been well studied in both melt- and solution-grown crystals by the ^{13}C–^{13}C DQ NMR approach.[28−33,37] It was found that the ^{13}C labeled isotactic poly(1-butene) (*i*PB1) with $\langle M_w \rangle$ = 37K g/mol[31,32] and poly(L-lactic acid) with $\langle M_w \rangle$ = 46K g/mol (*s*-PLLA)[37] form adjacent re-entry clusters in the solution-grown single crystals, and their sizes are independent of T_c while the morphologies drastically change under varied kinetics. Through two examples, it is demonstrated that there is no correlation between the chain-folding structure and morphology in the solution-grown crystals.[31,32,37]

Generally, chiral crystals such as *i*PB1 form III[29] and PLLA *α* form[37] adopt a looser packing structure than those of racemic crystals, e.g., form I of *i*PB1.[31] The chiral crystals induce lower ^{13}C spin densities than those in the racemic crystals. Therefore, the DQ signals in the chiral crystals are sensitive to dimensions of the folded chain clusters.[29,31,37] As a result, it was suggested that the small molecular weight *i*PB1 form III and PLLA adopt the nanoclusters consisting of adjacent re-entry structure in double or triple rows in the solution-grown crystals, and the cluster size is smaller than the size expected from the chain lengths.[29,37] On the basis of the recent NMR results, we naturally have a following question: How does the molecular weight affect the chain-folding structure of semicrystalline polymers in the solution-grown crystals? More specifically, does the size and the shape of the nanoclusters change depending on molecular weight and/or kinetics? To the best of our knowledge, however, there are few reports on detailed chain-level structure in the solution-grown crystals as functions of both $\langle M_w \rangle$ and kinetics.[5,17]

To answer above questions, ^{13}C 30% CH_3 labeled PLLA with different molecular weights, $\langle M_w \rangle$ = 90K and 326K g/mol, were newly synthesized in this work. Effects of both $\langle M_w \rangle$ and kinetics on the chain-folding structures and morphology of PLLA in the solution-grown crystals were investigated by ssNMR and AFM, respectively. Through the chain level-structure as well as morphology as a function of $\langle M_w \rangle$ and kinetics, crystallization mechanisms of polymers with different chain lengths were discussed.

2. RESULTS AND DISCUSSION

2.1. ^{1}H Solution- and ^{13}C Solid-State NMR Spectra for ^{13}C Labeled PLLA. In this study, ^{13}C labeled PLLA was polymerized by ring-opening polymerization of ^{13}C labeled lactide.[38] Addition of *n*-octanol with different amounts in polymerization[38] could control PLLAs with $\langle M_w \rangle$ = 90K g/mol (*m*) and 326K g/mol (*l*) in addition to $\langle M_w \rangle$ = 46 K g/mol (s) in our previous work.[37] (see details in the Experimental Section). To compare the structure of *s*-PLLA with those for *m*- and *l*-PLLA, we reintroduced some important results for *s*-PLLA[37] in this work.

Figure 1a–c shows the ^{1}H solution-state NMR spectra of ^{13}C CH_3 labeled *s*-, *m*-, and *l*-PLLA. In the solution state, ^{13}C CH_3 isotope labeling led to CH *J* coupling with J_{CH} = 122 Hz in addition to J_{HH} = 7 Hz. Thus, integrations of the CH_3 protons allowed us to determine the ^{13}C CH_3 isotope labeling ratios of 30 ± 1% for all *s*-, *m*-, and *l*-PLLA samples. The same ^{13}C labeling ratio for three samples is a key strategy for directly comparing the packing and chain-folding structure for them without calibrating the ^{13}C–^{13}C DQ simulation curves. Therefore, comparisons of the DQ buildup curves will directly provide detailed chain-folding structure for the PLLA samples with different $\langle M_w \rangle$s used in this work.

Figure 1d–f illustrates the ^{13}C CPMAS NMR spectra for ^{13}C CH_3 labeled *s*-, *m*-, and *l*-PLLA, respectively, in the solution-grown single crystals crystallized at T_c = 90 °C. As expected, the ^{13}C labeled CH_3 signal intensities were much higher than those for the CH and CO signals in natural abundance. The CH_3 signals showed doublet peaks with a intensity ratio of 4:1 at 17.1 and 16.4 ppm, respectively, which are characteristic

DOI: 10.1021/acs.macromol.8b01950
Macromolecules 2018, 51, 8729−8737

peaks for the stable α crystals, where the PLLA chains adopt 10_7 helical conformations in the orthorhombic lattice (see Figure 2).[39] The CH and CO groups also showed multiple

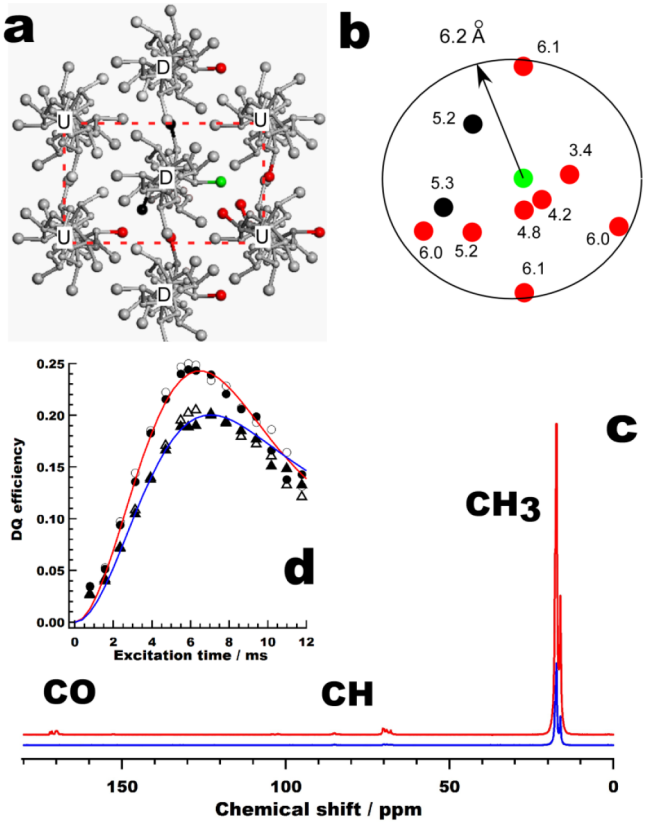

Figure 2. (a) Packing structure of the PLLA α crystal on the *ab*-plane, where the dashed red rectangle represented the crystal unit cell with a = 10.66, b = 6.16, and c = 28.88 Å.[39] (b) The 11 spin system was highlighted by colors. Green, black, and red filled circles represent reference, intrastem, and interstem spins at a distance within 6.2 Å from the reference spin. The number means a distance from the reference spin in units of Å. (c) ^{13}C CPMAS SQ and DQ NMR spectra for ^{13}C 30% CH_3 labeled *m*-PLLA α single crystals crystallized at T_c = 90 °C. The DQ excitation time was 6.27 ms. (d) DQ buildup curves for ^{13}C CH_3 labeled *m*-PLLA (filled circles and triangles), and *l*-PLLA α crystals (open circle and triangle) crystallized at 90 °C. The circles and triangles represent the DQ curves at 17.1 and 16.4 ppm, respectively. The solid curves were the simulated DQ curves based on the atomic positions and corresponding internuclear distance in (a, b) and T_2 of 9.5 ms.

splitting peaks due to the discrete conformation and packing structure.[40−43] The larger number of the CO and CH peaks means that CH and CO environments are more sensitive to the local structures than those of the CH_3 group. Even at T_c = ~0 °C, all three samples also adopted the same α crystals (see Figure S1). The experimentally available kinetics did not affect the packing selection of PLLA in the solution-grown crystals. The observed T_c independence of the packing structure in the solution-grown crystals was different from the reported T_c dependence of the α−α' packing selections in the melt-grown crystals.[42,43] To conclude the structural sources for different packing structures between the melt- and solution-grown crystals, we need to investigate the chain-folding structure in the melt-grown crystals.

For all three functional groups, a broad and structureless amorphous peak appeared at the bottom of the sharp crystalline peaks.[42,43] Among the three groups, the CO signal showed the largest contrasts in the line shapes between the amorphous and crystalline signals. Therefore, the CO signal was used for determination of the crystallinity, Φ. Five Gaussian peaks were applied to the observed CO crystalline peaks and one broad Gaussian peak to the amorphous peak. The determined crystallinity, Φ, of 0.58−0.60 is listed in Table 1. It was found that Φ was almost independent of $\langle M_w \rangle$ at the

Table 1. Crystallinity (Φ), Maximum Adjacent Re-Entry Number ($\langle n_{max} \rangle$), Mean Adjacent Re-Entry Number ($\langle n \rangle$), and Fraction of the Adjacent Re-Entry Structure in the Single Row in the Mixed Models with the Double Row ($\langle f \rangle_d$) and the Square Shape ($\langle f \rangle_s$) under the Assumption of Full Adjacent Re-Entry Structure of *s*-, *m*-, and *l*-PLLA Solution-Grown Crystals

	s-PLLA	*m*-PLLA	*l*-PLLA
Φ at T_c = 90 °C	0.60	0.60	0.58
Φ at T_c = ~0 °C	0.55	0.55	0.45
$\langle n_{max} \rangle$	16	32	117
$\langle n \rangle$	7[a]	7[a]	7[a]
$\langle f \rangle_d$	0.3	0.5	0.5
$\langle f \rangle_s$	0.4	0.6	0.65

[a]Adjacent re-entry number under the assumption of the double row.

small ΔT of 40 °C while Φ was dependent on $\langle M_w \rangle$ under the rapid quenched conditions. Reduction of mobility under quenching down to ~0 °C would lower Φ. Under such conditions, molecular weight significantly affected Φ.

2.2. Morphology of PLLA Crystals by AFM. Figure 1g−l depicts the AFM images of the PLLA solution-grown crystals as a function of T_c and $\langle M_w \rangle$. All *s*-, *m*-, and *l*-PLLA commonly showed faceted lozenge single crystals with a thickness of ca. 11 nm at T_c = 90 °C. These results are consistent with the reported results.[37,44] For *s*-PLLA, a complete lozenge shape was observed while the *m*- and *l*-PLLA single crystals showed truncations at the tips of the long axis. The PLLA crystal density (1.26 g/cm^3)[39] is close to that for the glassy state (1.25 g/cm^3).[45] Moreover, Raman spectroscopy suggested that PLLA in the glassy state adopts similar helical conformation with that in the α crystals.[46] Assuming the PLLA chain in the amorphous region adopts the same density and conformation with those in the crystalline regions, the thickness of the crystal core and two amorphous layers for all *s*-, *m*-, and *l*-PLLA was estimated to be 7 and 2 nm, respectively, at ΔT = 40 °C. Note that our simple analysis did not include structures at the fold loop. Under the rapidly quenched condition, all three samples showed dendrites[13,47] with a significant thickness of 75−200 nm, which arose from the multiple layers structures. It is well recognized that the dendrite morphology originates from kinetics. The multiple-layer structure is also another kinetics effect. Probably, the single chains cannot fold in the same layer but stay in the multiple layers due to the kinetics reason. More detailed discussions will be given later.

For the rapidly quenched samples, single layer thickness could not be determined due to the multiple layers. Based on $\langle M_w \rangle$, the 10_7 helical conformation in the α crystals, and the single crystals thickness, the maximum adjacent re-entry number ($\langle n_{max} \rangle$) was estimated to be 16, 32, and 117 for *s*-, *m*-, and *l*-PLLA, respectively. The wide $\langle n_{max} \rangle$ range may allow

DOI: 10.1021/acs.macromol.8b01950
Macromolecules 2018, 51, 8729−8737

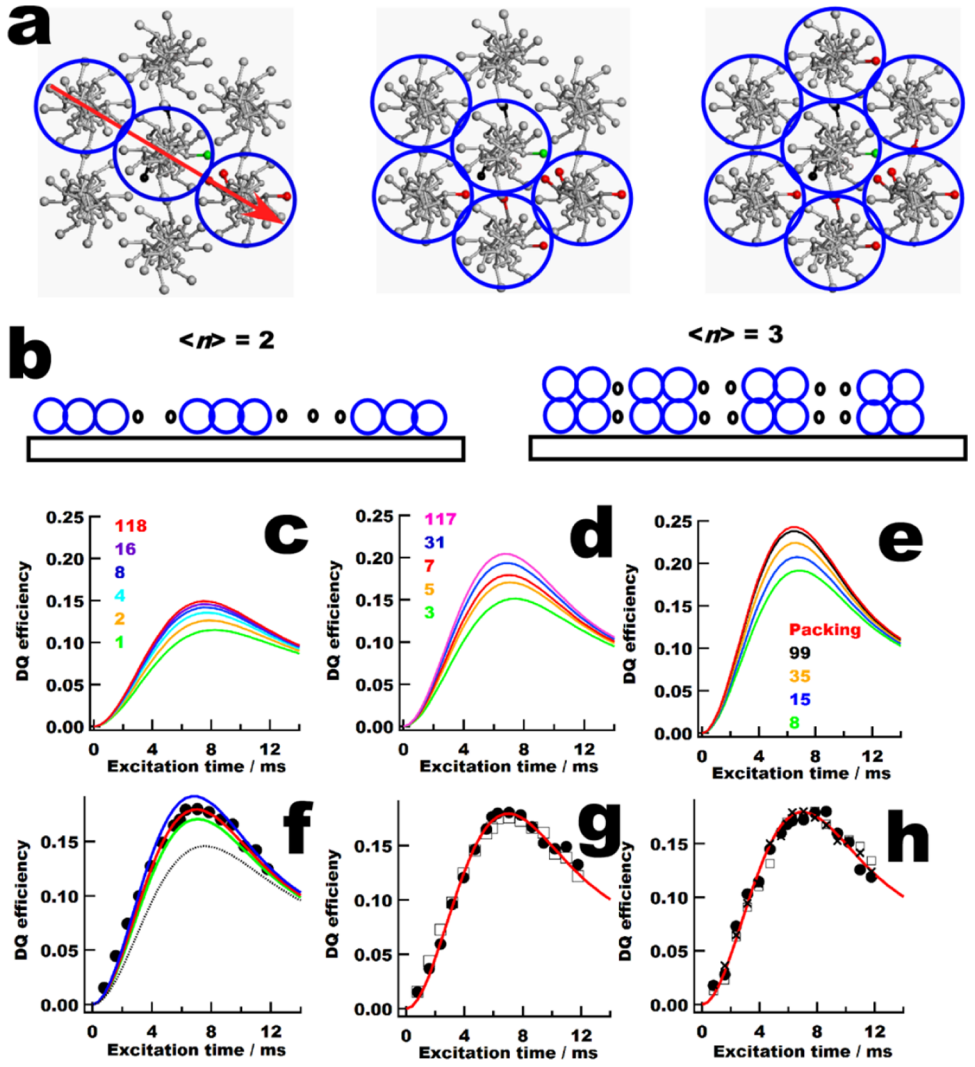

Figure 3. (a) Schematic illustrations of the chain-folding structures in the single (left), double (middle), and triple row (right) and corresponding spin systems including a reference spin colored by green and intrastem and interstem spins colored by black and red, respectively, at a distance within 6.2 Å. (b) Schematic illustrations for the chain-folding models with $\langle n \rangle$ = 2 and 3 in the single and double row, respectively, on an existing crystal surface. The simulated DQ buildup curves in (c) the single and (d) double row and (e) square shape as a function of $\langle n \rangle$. (f–h) Experimental DQ buildup curves for ^{13}C CH_3 labeled *s*-PLLA (filled circle in f and cross in h), *m*-PLLA (filled circle in g and h), and *l*-PLLA (open square in g and h) solution-grown crystals blends with nonlabeled PLLA with a mixing ratio of 1:9, crystallized at T_c = 90 °C (f, g) and T_c = ∼0 °C (h) in AA solution and the simulated curves based on (f) $\langle n \rangle$ = 16 in the single row (black dotted line), (f) $\langle n \rangle$ = 5 (green solid line), (f–h) $\langle n \rangle$ = 7 (red) in the double row, and (f) $\langle n \rangle$ = 8 in the triple row (blue).

us to understand crystallization mechanisms of the polymer chains in solution-grown crystals in the same solution with a fixed concentration of 0.05 wt % under the same kinetics.

2.3. Packing Structure of PLLA Crystals Analyzed by ^{13}C–^{13}C DQ NMR. Figure 2a illustrates the packing structure of the orthorhombic α crystals in the unit cell with a = 10.66, b = 6.16, and c = 28.88 Å determined by Sasaki et al.,[39] where the PLLA stems adopt left handed 10_7 helices having discrete conformations at five sites. The PLLA stems adopt upward and downward orientations at the four corners and the center, respectively, in the unit cell. DQ NMR spectroscopy excited ^{13}C–^{13}C spin pairs in multiple spins system of the ^{13}C 30% CH_3 labeled PLLA chains. The dipolar interaction is inversely proportional to the cube of the internuclear distance, and thus the short $^{13}CH_3$–$^{13}CH_3$ internuclear distances <7 Å were used in the structural analysis.

The single quantum (SQ, top) and DQ (bottom) ^{13}C CPMAS NMR spectra of ^{13}C CH_3 labeled *m*-PLLA single crystals crystallized at ΔT = 40 °C are plotted in Figure 3c. The DQ signal was excited by using the PostC7[25] sequence with a radio-frequency field strength of 35.7 kHz at a MAS frequency of 5102 Hz[28] (see details in the Experimental Section). The DQ efficiency ξ was defined as the intensity ratio of the peaks between the DQ and SQ signals. The experimental DQ curves at 17.4 ppm (circle) and 16.1 ppm (triangle) for ^{13}C 30% CH_3 labeled *m*-PLLA (filled circle and triangle) and *l*-PLLA (open circle and triangle) are illustrated in Figure 3d. In both samples, the DQ curves at 17.1 ppm were faster and higher than those at 16.4 ppm.[37]

In our previous work, a 11–12 spins system including a reference spin and surrounding 10–11 spins at a distance within 6.2 Å was used to approximately simulate the experimental DQ curves.[37] The atomic coordinates of the CH_3 carbons in the α crystals determined by XRD[39] were used

DOI: 10.1021/acs.macromol.8b01950
Macromolecules 2018, 51, 8729–8737

in our simulation. Among five sites, one system consisting of maximum 11 spins on the *ab*-plane is depicted in Figure 3a,b. The carbon colored by green was a reference spin which was surrounded by 10 spins at a distance less than 6.2 Å. The DQ buildup curves between a reference and one of surrounding spins were numerically simulated using SPINEVOUTION.[47] At each of the five sites, 2036 or more DQ buildup curves were simulated. Then, one average curve at each site among the five was obtained by weighting individual curves statistically. Finally, the DQ curves for the signals at 17.1 and 16.4 ppm were generated by averaging four fast curves and averaging two slow curves, respectively, under the assumption of T_2 = 9.5 ms (see more details in ref 37). These simulated curves could reproduce the experimental data for *s*-PLLA in our previous work[37] and are currently plotted in Figure 2d. These simulated curves well reproduced the experimental curves for both *m*- and *l*-PLLA at both 17.1 and 16.4 ppm. The consistency between the experimental and simulated DQ curves indicates that all three samples adopt the same CH_3-CH_3 distances. This is the first NMR report for the same packing structure of the semicrystalline polymers with different $\langle M_w \rangle$s. The consistency of the DQ curves in three samples indicates accuracy of the NMR data for the packing analysis.

2.4. Chain-Folding Structure as Functions of $\langle M_w \rangle$ and Kinetics. In a diluted blend system with nonlabeled chains, a ^{13}C labeled chain locally selects a certain spin system among maximum 11−12 spins based on its own trajectory. Figure 3a explains a basic concept for the spin selection via the chain trajectory using the same reference spin used in the packing analysis (Figure 2a,b).

In the case of chain folding in the single row along (−1, 1, 0) (Figure 3a), the reference spin (green) interacted with two (black) and three spins (red) in the same stem and the neighboring stems, respectively, within the same chain. Thereby, the 11 spin system used in the packing analysis was reduced down to 6 spins in the single row. Similarly, the double row as illustrated in Figure 3a (middle) generates 9 spins, and the triple row leads to 11 spins. The last one was the same with the spin system in the packing structure. In the case of the folding analysis, a boundary effect between the labeled and nonlabeled stems arising from the cluster size of the adjacent re-entry number and the statistical effect of the 10% labeled chains in the blend were taken into consideration.

In our previous works, two parameters of a mean value of the successive adjacent re-entry number, $\langle n \rangle$, and a mean value of the adjacent re-entry fraction, $\langle F \rangle$, were introduced.[28−37] $\langle F \rangle$ = 100% means that all the stems participate in the adjacent re-entry structure. In this paper, we treated with only $\langle F \rangle$ = 100% and thus no longer used $\langle F \rangle$ in our fitting parameters. For example, the chain trajectory with $\langle n \rangle$ = 2 in the single row and $\langle n \rangle$ = 3 in the double row are schematically illustrated in Figure 3b. Each cluster was connected via a long loop. The DQ NMR is a local probe and thus the interactions between different clusters can be ignored. Note that the adjacent re-entry fraction, P_{ar}, defined by Hoffman and co-workers[9] and others[6] corresponds to $\langle n \rangle/(\langle n \rangle + 1)$ in the present work, where $\langle n \rangle + 1$ means a mean value of stem number per one cluster, $\langle m \rangle$, formed via adjacent re-entry. $\langle n \rangle$ = 2 and 3 corresponds to P_{ar} = 0.67 and 0.75, respectively.

As described above, *s*-, *m*-, and *l*-PLLA samples gave $\langle n_{max} \rangle$ = 16, 32, and 118. Thus, it is interesting to illustrate the effects of the $\langle n \rangle$ values in the different row numbers on the DQ curves. Figure 3c,d,e depicts the simulated DQ curves for the adjacent re-entry model in the single, double row, and square shape, respectively, as a function of $\langle n \rangle$. In the single row, a maximum DQ efficiency, ξ_{max}, was 0.115, 0.135, 0.145, 0.148, and 0.149 for $\langle n \rangle$ = 1, 4, 16, 32, and 118, respectively. The simulated DQ curves sensitively changed their heights in the range of $\langle n \rangle \leq$ 16, while they were almost saturated at $\langle n \rangle \geq$ 16. Because the DQ NMR counts affect the folding ends on the DQ curve, large $\langle n \rangle$ values do not affect the DQ curves. In the double row, we calculated the DQ curves for only odd number for $\langle n \rangle$. ξ_{max} ranged between 0.151 at $\langle n \rangle$ = 3 and 0.204 at $\langle n \rangle$ = 117. Interestingly, $\langle n \rangle$ = 3 in the double row generated a slightly higher DQ curve than that for $\langle n \rangle$ = 118 in the single row. In the square shape of $\langle m \rangle \times \langle m \rangle$, where $\langle m \rangle$ is the stem number on one side, $\langle n \rangle$ = 8 in the triple row gave ξ_{max}= 0.191 at τ_{ex} = 6.64 ms, which was slightly lower than that for $\langle n \rangle$ = 117 in the double row. With increasing $\langle n \rangle$ to 99 in the square shape (10 × 10), ξ_{max} was 0.23 at τ_{ex} = 6.27 ms, which was almost the same as ξ_{max} in the packing structure (infinite square model) as depicted in Figure 2d. Thereby, in the case that a single molecule makes a single crystal, even a diluted blend sample showed a very high ξ_{max} value close to that in the nondiluted system.

From these perspective simulations, it is understood that the DQ NMR cannot precisely recognize larger $\langle n \rangle$ values larger than 16 in the single row but is sensitive to the mean cluster shapes, single, double, or higher rows. Thereby, it is challenging for ssNMR to precisely characterize a high $\langle M_w \rangle$ sample. However, the obtained information is particularly useful for discussing crystallization mechanisms of polymer chains as functions of both $\langle M_w \rangle$ and kinetics.

In our previous work, ^{13}C CH_3 labeled *s*-PLLA chains were blended with nonlabeled chains with a mixing ratio of 1:9 and crystallized at ΔT = 40 °C.[37] The chain-folding structure of the ^{13}C labeled chains in the blend single crystals were investigated by the DQ NMR. The observed DQ curve with ξ_{max} = 0.18 (black filled circle) as shown in Figure 3f was higher by ca. 0.03 than the simulated curve for the upper limit of $\langle n_{max} \rangle$ = 16 in the single row along the single crystal facet, e.g., (−1, 1, 0) plane (black dashed curve, Figure 3f). The simulated curves based on $\langle n \rangle$ = 5 in the double row (green curve in Figure 3f) and $\langle n \rangle$ = 8 in the triple row (blue curve) were closer to the experimental curve and the curve based on $\langle n \rangle$ = 7 in the double row (red curve) showed the best fit with the experimental curve.

The experimental DQ curves for the ^{13}C labeled *m*-PLLA (filled circle) and *l*-PLLA (open square) crystals blends with a nonlabeled sample at ΔT = 40 °C are illustrated in Figure 3g. Two experimental curves almost overlapped with each other. The simulated DQ curves for the *s*-PLLA experimental curve in Figure 3f could well reproduce the ones with the higher $\langle M_w \rangle$ samples without changing any parameters.

The DQ buildup curves for ^{13}C labeled *s*-PLLA (cross), *m*-PLLA (filled circle), and *l*-PLLA (open square) solution crystals blended with a nonlabeled chains prepared by a deep quenching down to ∼0 °C are depicted in Figure 3h. Surprisingly, the DQ curves for all three samples were well consistent with each other as well as those at ΔT = 40 °C.

In the real cases, mixed models of the different clusters might be involved in the single crystals. Here, we simply considered two mixed models of the chain-folding structures under the assumption of full adjacent re-entry structure. One model consisted of the single and double rows. By changing the fraction of the single row in the mixed model with the

DOI: 10.1021/acs.macromol.8b01950
Macromolecules 2018, 51, 8729−8737

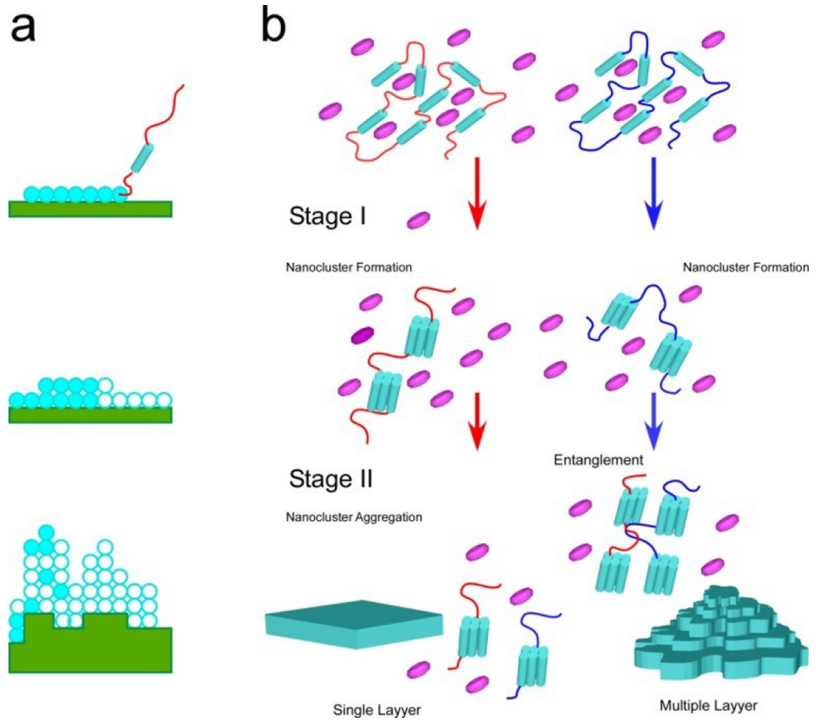

Figure 4. Schematic illustrations of the chain-folding mechanisms and structures induced via (a) secondary nucleation[7−9] in regime I (left, top), II (left, middle), and III (left, bottom) and (b) via primary nucleation,[10−13] In secondary nucleation, the nucleation and growth process is dominated by kinetics and leads to T_c dependence of the chain-folding structure. In the primary nucleation model, worse solvent−polymer interaction expels solvent molecules from the volume occupied by polymers and solvents and induces the nanocluster via folding (stage I). Aggregation process of the nanoclusters depends on kinetics and thus leads to the morphological change (stage II).

double row, $\langle f \rangle_d$, to the whole folding structure, the experimental curves were generated in terms of $\langle f \rangle_d$ = 0.3, 0.5, and 0.5 for *s*-, *m*-, and *l*-PLLA, respectively (see Figure S2). Another was a mixed model of the single row and square shape. As mentioned above, the square shape showed the highest DQ curve among various folding models. Combinations of the single row and square shape gave $\langle f \rangle_s$ of 0.4, 0.6, and 0.65 for *s*-, *m*-, and *l*-PLLA, respectively (see details in Figure S2). These values are listed in Table 1.

2.5. Crystallization Mechanism. Through systematic data on the chain-level structure as well as the morphology as functions of kinetics and $\langle M_w \rangle$, crystallization mechanisms of polymer chains with varied chain lengths in dilute solutions are discussed here.

The LH theory[7−9] predicts that secondary nucleation and growth driven by kinetics determines overall kinetics of the crystal growth and morphological differences: In regime I, stem deposition on the growth front initiates secondary nucleation and growth via reeling in polymer chains (Figure 4a, top). It is expected that a low ΔT and a small $\langle M_w \rangle$ sample lead to the full adjacent re-entry structure in the single row and resultantly leads to the faceted single crystals. With increasing ΔT, the probability to generate the secondary nucleation increases (regime II). Thus, a niche separation between the nucleation sites decreases with increasing ΔT. Multiple nucleation sites may limit the growth of chain folding in the single row and lead to collisions of two chains on the same plane. This process will depend on the chain length, polymer concentration, and ΔT. Collisions of two chains on the growth front generate an additional row via folding, which is called "superfolding".[5,6,15] With further increasing ΔT, the niche separation may correspond to a length of several stems (regime III), where a successive adjacent re-entry structure no longer exists due to participations of the multiple chains in the process. As a result, it is expected that the chain-folding structure highly depends on both ΔT and $\langle M_w \rangle$ in the solution-grown crystals, and changes of the folding directions and numbers induce dendrites and circular morphologies (kinetic roughness).

As demonstrated above, two mixed models could reproduce the experimental data under the assumption of full adjacent re-entry ($\langle f \rangle_{d \text{ or } s}$ = 0.3−0.65). One model consists of the single row and square cluster. It is assumed that the single row is a resultant structure via secondary nucleation while the square shape originates from primary nucleation. Another model is single and double rows. The chain-folding structure in the double row might be attributed to regime II. However, even these mixed models cannot explain invariant DQ results in wide ranges of $\langle M_w \rangle$ and ΔT. Thereby, the observed ΔT and $\langle M_w \rangle$ independences of the DQ results disprove the chain-folding structure induced via the secondary nucleation as the main mechanism and instead support the chain-folding cluster induced by the primary nucleation.

It is recognized that the poor polymer−solvent interaction plays an important role for crystallization in the dilute solution. Lowering the temperature from dissolution temperature, T_d, to T_c leads to a worse solvent−polymer affinity, which might be a driving force to expel solvent molecules from volumes co-occupied by polymer chains and solvent molecules. A weak polymer−polymer interaction induces self-aggregations accompanying folding, conformational ordering, and parallel arrangements (stage I in Figure 4b). To minimize the surface free energy, folding induces the nanocluster in the multiple rows. This process may not be a single step but complex process.

DOI: 10.1021/acs.macromol.8b01950
Macromolecules 2018, 51, 8729−8737

However, ssNMR cannot capture active process of chain folding in the dilute solution.

Recently, Kumaki et al. investigated the chain-folding structure of isotactic poly(methyl methacrylate) (*i*PMMA) Langmuir−Blodgett (LB) film blends with oligomers by using AFM.[20,21] They directly visualized the necklace structure of high molecular weight *i*PMMA, where oligomers in the LB film may behave like solvent molecules in the dilute solution. The structure of *i*PMMA directly observed by AFM is similar to the nanoclusters of PLLA and *i*PB1 after crystallization suggested by current and recent ssNMR studies.[29,31,32,37]

The aggregation process occurs in stage II and is dominated by the kinetics. Under the low ΔT, locally formed nanoclusters will be well aggregated with each other and leads to the faceted single crystals (Figures 1g−i and 4b, bottom). From the mean structure of the nanoclusters, it is speculated that deposition of the nanoclusters of multiple chains are involved in the aggregation process. Under the large ΔT, not only local formation of the nanoclusters but also large scale segregations between overall chains and solvent molecules may induce entanglements of the multiple chains even in the dilute solution. As a result, aggregation of the nanoclusters in the different layers results in three-dimensional dendrite morphology (Figures 1j−l and 4, right bottom).

Through current and recent works, it is emphasized that the dominant structural unit of polymer in solution crystallization is not a stem but a nanocluster formed via folding. The formation process of the nanocluster is very fast in dilute solution and thus is not affected by the experimentally used kinetics (stage I in Figure 4b). On the other hand, the aggregation process of the nanoclusters is dominated by kinetics and thus leads to the morphological difference as a function of kinetics (stage II in Figure 4b). Such a two-step mechanism is well consistent with the bundle and aggregation models[10−13] proposed in the solution-grown crystals.

Similar experimental results have been recently reported in solution crystallization of small and large organic molecules.[49,50] Marchenkova et al. using small-angle X-ray scattering (SAXS) investigated solution crystallization of a protein, lysozyme.[50] They observe a noticeable presence of dimers and octomers in addition to monomers in the early stage of crystallization. The results indicate that a high probability that the crystal unit is combined from eight molecules of lysozyme. Thereby, formation of the nanoblock structure might be common features in crystallization of organic molecules in the solution state.

The proposed two-step crystallization of polymer in the dilute solution might also be the similar process with multistage model of polymer in the melt-grown crystals proposed by Strobl,[51] where the clusters gradually change their internal structures as a function of time. In the melt-grown crystals, entanglements of polymer chains significantly affect the folding events. In fact, Hong et al. reported $\langle n \rangle$ = 1.7−2 of *i*PB1 in the melt-grown crystals,[31] which is much shorter than in the solution-grown crystals ($\langle n \rangle$ = 7). Thereby, the cluster size of the same chain is largely reduced from that in the solution-single crystals. To further understand the crystallization process of polymer in the melt-grown crystals, we are currently investigating kinetics and $\langle M_w \rangle$ effects on the chain-folding and packing structures of PLLA in the melt-grown crystals. These results will be reported elsewhere in the near future.

3. CONCLUSION

In the present work, the morphology and chain-folding structures of ^{13}C 30% CH_3 labeled PLLA samples with $\langle M_w \rangle$ of 46K, 90K, and 326K g/mol solution-grown crystals in dilute amyl acetate solution were successfully investigated as a function of ΔT. It was demonstrated that the morphology highly depended on kinetics but was independent on $\langle M_w \rangle$: Faceted lozenge single crystals with a thickness of ca. 11 nm were commonly formed at ΔT = 40 °C while the large ΔT of ∼130 °C resulted in kinetically dominant dendrite crystals consisting of the multiple layers. By comparison of the experimental and simulated DQ curves, it was found that a mean structure of the folded chains clusters was independent on both $\langle M_w \rangle$ and experimentally used kinetics. The results indicated that worse solvent−polymer affinity induces local segregations between the polymer and solvent molecules and formation of the nanoclusters (stage I) and aggregations of the nanoclusters (stage II). The proposed mechanisms disprove classical secondary nucleation theory.

4. EXPERIMENTAL SECTION

4.1. Synthesis of PLLA. ^{13}C CH_3 labeled L-lactic acid (1 g, L-LA, Sigma-Aldrich) and 2.33 g of nonlabeled L-LA were dissolved in 600 mg of water. The water was removed at 110 °C for 2 h, and then the oligomers were produced at 140 °C for 8 h under vacuum. The catalyst of Al_2O_3 and $Sn(Oct)_2$ (80 mg) with a weight ratio of 1:4 was added for the degradation of the oligomers to obtain 30% ^{13}C CH_3 labeled cyclic lactide at 200 °C. The lactide was distilled out of the reaction system and purified by precipitating the acetone solution in ice−water. 30% ^{13}C CH_3 labeled and nonlabeled PLLA were synthesized by the ring-opening polymerization of the ^{13}C CH_3 labeled and nonlabeled lactide, respectively, at 140 °C.[38] The molecular weight was characterized by gel permeation chromatography (GPC, Tosoh Instrument) with an IR detector in tetrahydrofuran (THF) eluent (1 mL/min, 40 °C). *n*-Octanol with concentrations of 0.26, 0.13, and 0.06% was used as the initiator to control the weight-average molecular weight, $\langle M_w \rangle$, of 46K (*s*), 90K (*m*), and 326K g/mol (*l*) for ^{13}C labeled PLLA, respectively. Similarly, $\langle M_w \rangle$s of nonlabeled *s*-, *m*-, and *l*-PLLA were 47K, 88K, and 239K g/mol, respectively.

4.2. Preparation of Solution-Grown Crystals. PLLA (15 mg) was dissolved in 30 g of amyl acetate (AA) solution (0.05 wt %) at 130 °C (T_d) for 30 min. The solution was quickly transferred to another oil bath set at T_c = 90 or 0 °C. ΔT was defined as $T_d - T_c$. The solution crystallization was conducted for 24 h. Finally, the precipitated crystals were filtered and dried under vacuum for 1 day.

4.3. NMR and AFM Characterization. Atomic force microscope (AFM, Bruker Nano) in the tapping mode was chosen to observe the crystal morphology. The scanning rate was set as 1 Hz with a resolution of 512 pixels. The AFM samples were prepared by dropping the crystal suspensions onto the silicon wafer and desiccated under vacuum prior to the measurement. The solution ^1H NMR experiments were conducted on a Varian Mercury 300 with a relaxation delay of 10 s at 25 °C. Deuterated $CDCl_3$ and tetramethylsilane (TMS) were used as solvent and the internal reference of ^1H chemical shift, respectively. ssNMR experiments were conducted on a BRUKER AVANCE 300 with a 4 mm double resonance MAS probe at 25 °C. The MAS frequency was set to 5102 ± 5 and 10000 ± 5 Hz. The 90° pulses for ^1H and ^{13}C were adjusted to 2.4 and 4.8 μs, respectively. The recycle delay and cross-polarization (CP) time were set as 2 s and 1 ms, respectively. The PostC7[25] sequence with a field strength of 35.7 kHz at the MAS frequency of 5102 Hz was used to excite and reconvert $^{13}C-^{13}C$ DQ signals into single quantum (SQ) signals. ^1H two-pulse phase modulation (TPPM)[52] and continuous wave decoupling with a field strength of 104 kHz were applied to the ^1H channel during the ^{13}C

DOI: 10.1021/acs.macromol.8b01950
Macromolecules 2018, 51, 8729−8737

acquisition and recoupling periods, respectively. Spin dynamics simulations were conducted by SPINEVOLUTION.[48]

■ ASSOCIATED CONTENT

Supporting Information

The Supporting Information is available free of charge on the ACS Publications website at DOI: 10.1021/acs.macromol.8b01950.

Figures S1 and S2 (PDF)

■ AUTHOR INFORMATION

Corresponding Authors

*(Y.H.) E-mail: yh31@zips.uakron.edu.
*(T.M.) E-mail: miyoshi@uakron.edu.

ORCID

Yang Zhou: 0000-0002-4276-6253
You-lee Hong: 0000-0001-8568-9828
Toshikazu Miyoshi: 0000-0001-8344-9687

Notes

The authors declare no competing financial interest.

■ ACKNOWLEDGMENTS

This study was financially supported by the National Science Foundation (Grant DMR-1708999).

■ REFERENCES

(1) Keller, A. A. Note on Single Crystals in Polymers: Evidence for a Folded Chain Configuration. *Philos. Mag.* **1957**, *2*, 1171−1175.
(2) Cheng, S. Z. D. *Phase Transitions in Polymers: The Role of Metastable States*, 1st ed.; Elsevier: Amsterdam, 2008.
(3) Lotz, B.; Miyoshi, T.; Cheng, S. Z. D. 50th Anniversary Perspective : Polymer Crystals and Crystallization: Personal Journeys in a Challenging Research Field. *Macromolecules* **2017**, *50*, 5995−6025.
(4) Ungar, G.; Zeng, X. B. Learning Polymer Crystallization with the Aid of Linear, Branched and Cyclic Model Compounds. *Chem. Rev.* **2001**, *101*, 4157−4188.
(5) Sadler, D. M.; Keller, A. Neutron Scattering of Solution-Grown Polymer Crystals: Molecular Dimensions Are Insensitive to Molecular Weight. *Science* **1979**, *203*, 263−265.
(6) Spells, S. J.; Sadler, D. M. Neutron Scattering Studies on Solution-Grown Crystals of Polyethylene: A Statistical Preference for Adjacent Re-Entry. *Polymer* **1984**, *25*, 739−748.
(7) Lauritzen, J. I.; Hoffman, J. D. Theory of Formation of Polymer Crystals with Folded Chains in Dilute Solution. *J. Res. Natl. Bur. Stand., Sect. A* **1960**, *64A*, 73.
(8) Hoffman, J. D.; Lauritzen, J. I. Crystallization of Bulk Polymers With Chain Folding : Theory of Growth of Lamellar Spherulites. *J. Res. Natl. Bur. Stand., Sect. A* **1961**, *65A*, 297.
(9) Hoffman, J. D.; Miller, R. L. Kinetic of Crystallization from the Melt and Chain Folding in Polyethylene Fractions Revisited: Theory and Experiment. *Polymer* **1997**, *38*, 3151−3212.
(10) Allegra, G.; Famulari, A. Chain Statistics in Polyethylene Crystallization. *Polymer* **2009**, *50*, 1819−1829.
(11) Allegra, G.; Meille, S. V. Pre-Crystalline, High-Entropy Aggregates: A Role in Polymer Crystallization? *Adv. Polym. Sci.* **2005**, *191*, 87−135.
(12) Liu, C.; Muthukumar, M. Langevin Dynamics Simulations of Early-Stage Polymer Nucleation and Crystallization. *J. Chem. Phys.* **1998**, *109*, 2536−2542.
(13) Zhang, J.; Muthukumar, M. Monte Carlo Simulations of Single Crystals from Polymer Solutions. *J. Chem. Phys.* **2007**, *126*, 234904.
(14) Yoon, D. Y.; Flory, P. J. Molecular Morphology in Semicrystalline Polymers. *Faraday Discuss. Chem. Soc.* **1979**, *68*, 288.
(15) Sadler, D. M. Neutron Scattering by Crystalline Polymers: Molecular Conformations and Their Interpretation. In *Structure of Crystalline Polymers*; Hall, I. H., Ed.; Elsevier Applied Science: 1984; pp 125−180.
(16) Keller, A. Crystalline Polymers; an Introduction. *Faraday Discuss. Chem. Soc.* **1979**, *68*, 145−166.
(17) Cheam, T. C.; Krimm, S. Mixed-Crystal Infrared Studies of Chain-Folding in Polyethylene Single Crystals: Low-Temperature and Molecular Weight Studies. *J. Polym. Sci., Polym. Phys. Ed.* **1981**, *19*, 423−447.
(18) Jing, X.; Krimm, S. Mixed-Crystal Infrared Studies of Chain Folding in Polyethylene Single Crystals : Effect of Crystallization Temperature. *J. Polym. Sci., Polym. Phys. Ed.* **1982**, *20*, 1155−1173.
(19) Spells, S. J.; Sadler, D. M.; Keller, A. Chain Trajectory in Solution Grown Polyethylene Crystals: Correlation between Infra-Red Spectroscopy and Small-Angle Neutron Scattering. *Polymer* **1980**, *21*, 1121−1128.
(20) Kumaki, J.; Kawauchi, T.; Yashima, E. Two-Dimensional Folded Chain Crystals of a Synthetic Polymer in a Langmuir-Blodgett Film. *J. Am. Chem. Soc.* **2005**, *127*, 5788−5789.
(21) Anzai, T.; Kawauchi, M.; Kawauchi, T.; Kumaki, J. Crystallization Behavior of Single Isotactic Poly (Methyl Methacrylate) Chains Visualized by Atomic Force Microscopy. *J. Phys. Chem. B* **2015**, *119*, 338−347.
(22) Mullin, N.; Hobbs, J. K. Direct Imaging of Polyethylene Films at Single-Chain Resolution with Torsional Tapping Atomic Force Microscopy. *Phys. Rev. Lett.* **2011**, *107*, 197801.
(23) Liu, K.; Song, Y.; Feng, W.; Liu, N.; Zhang, W.; Zhang, X. Extracting a Single Polyethylene Oxide Chain from a Single Crystal by a Combination of Atomic Force Microscopy Imaging and Single-Molecule Force Spectroscopy: Toward the Investigation of Molecular Interactions in Their Condensed States. *J. Am. Chem. Soc.* **2011**, *133*, 3226.
(24) Wittmann, J. C.; Lotz, B. Polymer Decoration: The Orientation of Polymer Folds As Revealed By the Crystallization of Polymer Vapors. *J. Polym. Sci., Polym. Phys. Ed.* **1985**, *23*, 205−226.
(25) Hohwy, M.; Jakobsen, H. J.; Edén, M.; Levitt, M. H.; Nielsen, N. C. Broadband Dipolar Recoupling in the Nuclear Magnetic Resonance of Rotating Solids: A Compensated C7 Pulse Sequence. *J. Chem. Phys.* **1998**, *108*, 2686−2694.
(26) Caporini, M. A.; Bajaj, V. S.; Veshtort, M.; Fitzpatrick, A.; MacPhee, C. E.; Vendruscolo, M.; Dobson, C. M.; Griffin, R. G. Accurate Determination of Interstrand Distances and Alignment in Amyloid Fibrils by Magic Angle Spinning NMR. *J. Phys. Chem. B* **2010**, *114*, 13555−13561.
(27) Mehta, M. A.; Eddy, M. T.; McNeill, S. A.; Mills, F. D.; Long, J. R. Determination of Peptide Backbone Torsion Angles Using Double-Quantum Dipolar Recoupling Solid-State NMR Spectroscopy. *J. Am. Chem. Soc.* **2008**, *130*, 2202−2212.
(28) Hong, Y. L.; Miyoshi, T. Chain-Folding Structure of a Semicrystalline Polymer in Bulk Crystals Determined by C-13-C-13 Double Quantum NMR. *ACS Macro Lett.* **2013**, *2*, 501−505.
(29) Hong, Y. L.; Yuan, S.; Li, Z.; Ke, Y.; Nozaki, K.; Miyoshi, T. Three-Dimensional Conformation of Folded Polymers in Single Crystals. *Phys. Rev. Lett.* **2015**, *115*, 1−5.
(30) Hong, Y.; Chen, W.; Yuan, S.; Kang, J.; Miyoshi, T. Chain Trajectory of Semicrystalline Polymers As Revealed by Solid-State NMR Spectroscopy. *ACS Macro Lett.* **2016**, *5*, 355−358.
(31) Hong, Y.; Koga, T.; Miyoshi, T. Chain Trajectory and Crystallization Mechanism of a Semicrystalline Polymer in Melt- and Solution-Grown Crystals As Studied Using 13 C− 13 C Double-Quantum NMR. *Macromolecules* **2015**, *48*, 3282−3293.
(32) Hong, Y.; Miyoshi, T. Elucidation of the Chain-Folding Structure of a Semicrystalline Polymer in Single Crystals by Solid-State NMR. *ACS Macro Lett.* **2014**, *3*, 556−559.
(33) Li, Z.; Hong, Y.; Yuan, S.; Kang, J.; Kamimura, A.; Otsubo, A.; Miyoshi, T. Determination of Chain-Folding Structure of Isotactic Polypropylene in Melt-Grown α Crystals by 13 C−13 C Double

DOI: 10.1021/acs.macromol.8b01950
Macromolecules 2018, 51, 8729−8737

Quantum NMR and Selective Isotopic Labeling. *Macromolecules* **2015**, *48*, 5752−5760.
(34) Yuan, S.; Li, Z.; Hong, Y.; Ke, Y.; Kang, J.; Kamimura, A.; Otsubo, A.; Miyoshi, T. Folding of Polymer Chains in the Early Stage of Crystallization. *ACS Macro Lett.* **2015**, *4*, 1382−1385.
(35) Yuan, S.; Li, Z.; Kang, J.; Hong, Y.; Kamimura, A.; Otsubo, A.; Miyoshi, T. Determination of Local Packing Structure of Mesomorphic Form of Isotactic Polypropylene by Solid-State NMR. *ACS Macro Lett.* **2015**, *4*, 143−146.
(36) Chen, W.; Wang, S.; Zhang, W.; Ke, Y.; Hong, Y.; Miyoshi, T. Molecular Structural Basis for Stereocomplex Formation of Polylactide Enantiomers in Dilute Solution. *ACS Macro Lett.* **2015**, *4*, 1264−1267.
(37) Wang, S.; Yuan, S.; Chen, W.; He, Q.; Hong, Y.; Miyoshi, T. Solid-State NMR Study of the Chain Trajectory and Crystallization Mechanism of Poly(l-Lactic Acid) in Dilute Solution. *Macromolecules* **2017**, *50*, 6404−6414.
(38) Kaihara, S.; Matsumura, S.; Mikos, A. G.; Fisher, J. P. Synthesis of Poly(L-Lactide) and Polyglycolide by Ring-Opening Polymerization. *Nat. Protoc.* **2007**, *2*, 2767−2771.
(39) Sasaki, S.; Asakura, T. Helix Distortion and Crystal Structure of the R -Form of Poly (L -Lactide). *Macromolecules* **2003**, *36*, 8385−8390.
(40) Thakur, K. a M.; Kean, R. T.; Zupfer, J. M.; Buehler, N. U.; Doscotch, M. A.; Munson, E. J. Solid State 13 C CP-MAS NMR Studies of the Crystallinity and Morphology of Poly (L -Lactide). *Macromolecules* **1996**, *29*, 8844−8851.
(41) Pawlak, T.; Jaworska, M.; Potrzebowski, M. J. NMR Crystallography of α-Poly(l-Lactide). *Phys. Chem. Chem. Phys.* **2013**, *15*, 3137−3145.
(42) Pan, P.; Yang, J.; Shan, G.; Bao, Y.; Weng, Z.; Cao, A.; Yazawa, K.; Inoue, Y. Temperature-Variable FTIR and Solid-State 13 C NMR Investigations on Crystalline Structure and Molecular Dynamics of Polymorphic Poly(l -Lactide) and Poly(l -Lactide)/Poly(d -Lactide) Stereocomplex. *Macromolecules* **2012**, *45*, 189−197.
(43) Chen, W.; Zhou, W.; Makita, Y.; Wang, S.; Yuan, S.; Konishi, T.; Miyoshi, T. Characterization of the Slow Molecular Dynamics of Poly(l-Lactic Acid) in α and A′ Phases, in a Glassy State, and in a Complex with Poly(d-Lactic Acid) by Solid-State NMR. *Macromol. Chem. Phys.* **2018**, *219*, 1700451.
(44) Zheng, J. X.; Xiong, H.; Chen, W. Y.; Lee, K.; Van Horn, R. M.; Quirk, R. P.; Lotz, B.; Thomas, E. L.; Shi, A. C.; Cheng, S. Z. D. Onsets of Tethered Chain Overcrowding and Highly Stretched Brush Regime via Crystalline - Amorphous Diblock Copolymers. *Macromolecules* **2006**, *39*, 641−650.
(45) Garlotta, D. A. Literature Review of Poly (Lactic Acid). *J. Polym. Environ.* **2001**, *9*, 63−84.
(46) Kang, S.; Hsu, S. L.; Stidham, H. D.; Smith, P. B.; Anne Leugers, M.; Yang, X. A Spectroscopic Analysis of Poly(Lactic Acid) Structure. *Macromolecules* **2001**, *34*, 4542−4548.
(47) Xu, H.; Matkar, R.; Kyu, T. Phase-Field Modeling on Morphological Landscape of Isotactic Polystyrene Single Crystals. *Phys. Rev. E* **2005**, *72*, 011804.
(48) Veshtort, M.; Griffin, R. G. SPINEVOLUTION: A Powerful Tool for the Simulation of Solid and Liquid State NMR Experiments. *J. Magn. Reson.* **2006**, *178*, 248−282.
(49) Erdemir, D.; Lee, A. Y.; Myerson, A. S. Nucleation of Crystals from Solution: Classical and Two-Step Models. *Acc. Chem. Res.* **2009**, *42*, 621−629.
(50) Kovalchuk, M. V.; Blagov, A. E.; Dyakova, Y. A.; Gruzinov, A. Y.; Marchenkova, M. A.; Peters, G. S.; Pisarevsky, Y. V.; Timofeev, V. I.; Volkov, V. V. Investigation of the Initial Crystallization Stage in Lysozyme Solutions by Small-Angle X-Ray Scattering. *Cryst. Growth Des.* **2016**, *16*, 1792−1797.
(51) Strobl, G. From the Melt via Mesomorphic and Granular Crystalline Layers to Lamellar Crystallites: A Major Route Followed in Polymer Crystallization? *Eur. Phys. J. E: Soft Matter Biol. Phys.* **2000**, *3*, 165−183.
(52) Bennett, A. E.; Rienstra, C. M.; Auger, M.; Lakshmi, K. V.; Griffin, R. G. Heteronuclear Decoupling in Rotating Solids. *J. Chem. Phys.* **1995**, *103*, 6951.

DOI: 10.1021/acs.macromol.8b01950
Macromolecules 2018, 51, 8729−8737